ROYAL SOCIETY OF CHEMISTRY

REVIEW

Check for updates

Chalcogenide-based inorganic sodium solid electrolytes

Huanhuan Jia,[ab] Linfeng Peng,[a] Chuang Yu,[a] Li Dong,*[c] Shijie Cheng[a] and Jia Xie ![ORCID] *[a]

All-solid-state sodium batteries (ASSSBs) are promising to be applied to large-scale energy storage systems due to the extensive source of raw materials, high safety, and high energy density. As one of the key materials for ASSSBs, sodium solid electrolytes (SSEs) have attracted significant attention in recent years. Therein, chalcogenide-based inorganic sodium solid electrolytes (ISSEs) stand out owing to their decent room temperature ionic conductivity and lower mechanical stiffness. The fundamental understanding of the structure–activity relationship is of great significance for guiding the design of chalcogenide-based ISSEs. In this review, we provide an overview of the research progress in chalcogenide-based ISSEs based on their crystal structures, synthetic methods, chemical/electrochemical properties, and structure–activity relationship, especially focusing on the perspective of crystal structure designs. We hope to provide some prospects and thoughts for the design of relevant solid electrolytes (SEs) in the future.

1. Introduction

Sodium batteries are considered one of the most promising candidates for next-generation energy storage technologies due to the highly abundant Na resource on the earth, low cost, and comparable electrochemical performances to current lithium-ion batteries.[1–5] Using beta-Al_2O_3 as a solid electrolyte (SE), the first applications of Na–S batteries and ZEBRA batteries were realized in 1967 and 1978 respectively.[6–8] In fact, high-temperature Na–S (sodium–sulfur) batteries using beta-Al_2O_3 have been commercialized and applied in stationary energy storage systems for decades.[2,9] However, ZEBRA batteries and Na–S batteries are usually operated at above 300 degree centigrade, below which molten Na and S cause high safety risk.[3,10] In recent years, much effort has been devoted to exploring electrode materials and electrolytes for building intermediate-temperature (IMT) and room temperature (RT) Na–S batteries.[9,11] At the same time, sodium-ion batteries using organic liquid electrolytes parallelly grown still suffer from safety issues due to the hidden danger of leakage, fire, and explosion. Thus the exploitation of solid-state sodium batteries operating at IMT or RT is an essential option for enhancing the security level.[9,12–16] Therein, exploring sodium solid electrolytes (SSEs) with high ionic conductivity at room temperature and lower interfacial resistance between the

[a]*State Key Laboratory of Advanced Electromagnetic Engineering and Technology, School of Electrical and Electronic Engineering, Huazhong University of Science and Technology, Wuhan 430074, China. E-mail: xiejia@hust.edu.cn*

[b]*State Key Laboratory of Materials Processing and Die & Mould Technology, School of Materials Science and Engineering, Huazhong University of Science and Technology, Wuhan 430074, China*

[c]*Naval University of Engineering, Wuhan 430033, China. E-mail: 12357609@qq.com*

Huanhuan Jia received her bachelor's degree from Lanzhou University in 2014. Then she continued her studies at the University of Science and Technology of China and received her master's degree in the major of Physical Chemistry in 2017. She is currently a Ph.D. candidate under the supervision of Prof. Jia Xie at the Huazhong University of Science and Technology. Her research interests focus on the design of novel chalcogenide-based sodium solid electrolytes.
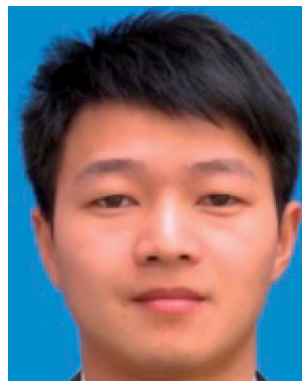
Linfeng Peng received his bachelor's degree in 2013 and received his master's degree in the major of Materials Processing Engineering in 2016 from the Wuhan Institute of Technology. He is currently a Ph.D. candidate under the supervision of Prof. Jia Xie at the Huazhong University of Science and Technology. His research interests focus on solid electrolytes and solid-state batteries.

electrode and electrolyte is critical to the development of all-solid-state sodium batteries with good electrochemical performance.[17–20]

Systematic research on inorganic sodium solid electrolytes (ISSEs) began from 1967, when beta-Al_2O_3 with high ionic conductivity was reported,[8,21,22] and it flourished after 2012. Current ISSEs mainly include various types of beta-Al_2O_3,[8,23–27] NACICON,[12,21,22,28–34] sulphide, antiperovskite[35–40] and compound hydride.[41–47] Among them, chalcogenide-based ISSEs usually have higher room temperature ionic conductivity, lower synthesis temperatures, and lower mechanical stiffness compared to oxides, and thus attract great attention.[48,49] As early as 1992, tetragonal Na_3PS_4 (t-Na_3PS_4) with an ionic conductivity of 4.17×10^{-6} S cm^{-1} at 50 °C was synthesized by solid-phase synthesis.[50] After that, cubic Na_3PS_4 (c-Na_3PS_4) with a room temperature ionic conductivity of 2×10^{-4} S cm^{-1} was reported by Hayashi et al., and was used in a combination of TiS_2 and a Na–Sn alloy to assemble ASSSBs, delivering a discharge capacity of 90 mA h g^{-1} after 10 cycles at room temperature.[51] Intensive research efforts have led to different chalcogenide-based Na ion conductors since then, including Na_3PnS_4,[50–56] Na_3PnSe_4 (Pn = P, Sb),[57–59] $Na_3As_{0.38}P_{0.62}S_4$,[60,61] $Na_{3-x}Pn_{1-x}W_xS_4$,[62,63] $Na_{11}Sn_2PS_{12}$,[64,65] $Na_{4-x}Sn_{1-x}Sb_xS_4$ and $Na_4Sn_{0.67}Si_{0.33}S_{12}$ ($Na_{12}Sn_2SiS_{12}$) and so on.[66–69] Therein, the room temperature ionic conductivity of $Na_{2.9}Sb_{0.9}W_{0.1}S_4$ is $(4.1 \pm 0.8) \times 10^{-2}$ S cm^{-1} which is the highest among the existing chalcogenide-based ISSEs and even surpasses that of many current liquid electrolytes.[63] However, only a few ISSEs achieve good battery performance in all ASSSBs on account of their undesirable chemical/electrochemical stability and poor compatibility with electrodes. Therefore, continuing research efforts, especially understanding the fundamental problem and structure–property relationship, is of great significance for optimizing and targeting the design of chalcogenide-based ISSEs.[70]

The present review summarizes an integrated analysis of the reported chalcogenide-based ISSEs from the perspective of crystal structure design, especially focusing on the intrinsic crystal structure and structure–activity relationship. We give an overview of chalcogenide-based ISSEs in Section 2 and summarize the relevant general synthesis methods in Section 3. Then the crystal structures and structural evolutions of the Na_3PS_4 type and $Na_{11}Sn_2PS_{12}$ type ISSEs are described in Section 4. Finally, a systematic analysis of the structure–activity relationships for the mentioned ISSEs is summarized in Section 5. It is aimed to provide some prospects and thoughts for the design of related SEs in the future.

Dr Chuang Yu received his Ph.D. degree in Material Chemistry from TU Delft (Delft, the Netherlands) in 2017. His current research interests focus on the synthesis and conduction mechanism of sulphide solid electrolytes and their applications in all-solid-state batteries.

Shijie Cheng received his Master's and PhD degree in Electrical Engineering from the Huazhong University of Science (HUST) and Technology and the University of Calgary in 1981 and 1986 respectively. He is currently a member of the Chinese Academy of Sciences and a full professor at the HUST. His research interests include power system stability analysis, power system control, energy storage systems and application of artificial intelligence in power systems.

Li Dong received his Master's degree in Mechanical Engineering from the National University of Defense Technology. He is now a lecturer at the Naval University of engineering. His research interests focus on energy systems and integrated support engineering.

Jia Xie received his Ph.D. in the Department of Chemistry from Stanford University. He is now a professor at the Huazhong University of Science and Technology. He was a Senior Researcher in Dow Chemical (USA) from 2008–2012 and the CTO of Hefei Guoxuan High-Tech Power Energy Co., Ltd from 2012–2015. His research interests focus on advanced energy storage materials and devices.

This journal is © The Royal Society of Chemistry 2021

J. Mater. Chem. A, 2021, **9**, 5134–5148 | **5135**

2. Overview of chalcogenide-based ISSEs

Solid electrolyte (SE) is regarded as a special crystal structure composed of a skeleton structure and mobile species.[71,72] The skeleton structure consists of polyanionic polyhedra, which stack to form rigid matrixes with one-dimensional, two-dimensional, or three-dimensional connected channels. The mobile species are distributed in the interstitial spaces in the structure.[21] Fig. 1a highlights the structural building elements for chalcogenide-based ISSEs in the periodic table. In general, the elements of group 14 or 15 are the main skeleton building elements, while S and Se are the main ligand atoms. The polyanionic polyhedra such as $[PS_4]^{3-}$, $[SbS_4]^{3-}$, and $[SnS_4]^{4-}$ are constructed to form the rigid matrix and the mobile species, Na^+, are distributed in the interstitial sites.[51,56,64] Aliovalent anion or cation doping/substitution is commonly used to introduce vacancies to enhance ionic conductivity or improve chemical/electrochemical stability.[62,68,73,74] The reported chalcogenide-based ISSEs are summarized and listed in Table 1, which can be divided into two categories according to the crystal structure, the Na_3PS_4 type and the $Na_{11}Sn_2PS_{12}$ type. These types are described by the pseudo ternary phase diagram shown in Fig. 1b and c respectively. The Na_3PS_4 type ISSEs showed in Fig. 1b represent ISSEs isostructural with Na_3PS_4, including the cubic phase belonging to the space group of $I\bar{4}3m$ and the tetragonal phase belonging to the space

group of $P\bar{4}2_1c$. The cations in these skeleton structures are mainly from group 15 elements (P, and Sb). The $Na_{11}Sn_2PS_{12}$ type ISSEs showed in Fig. 1c represent ISSEs isostructural with $Na_{11}Sn_2PS_{12}$, and belong to the space group of $I4_1/acd$. Two systems of $Na_{11}Sn_2PnCh_{12}$ (Pn = P, Sb; Ch = S, Se) and $Na_{12-x-y}[Sn_2Si]_{1-x}Pn_xS_{1-y}X_y$ (Pn = P, Sb; X = Cl, Br, I) are included. The detailed structural evolution of these two types of ISSEs will be discussed in Section 4.

3. Synthetic routes for chalcogenide-based ISSEs

As shown in Fig. 2a and b, the synthetic methods of chalcogenide-based ISSEs mainly include solid-phase methods and liquid-phase methods. The solid-phase synthesis is a common method to obtain chalcogenide-based ISSEs. As shown in Fig. 2a, there are two main routes in the solid-phase method, in which one contains a precursor mixing, mechanical ball milling process and subsequent sintering annealing process,[51,57,60,61,67–69,85] and another involves a simple precursor mixture and sintering annealing process.[54,64,83] For the synthesis of chalcogenide-based samples, the sintering temperature is relatively mild, which generally ranges from 200 °C to 800 °C.[51,57,64,85] Optimizing the synthetic conditions such as ball milling parameters and the sintering temperature can regulate the defect in the crystal and affect the crystal phase and ionic
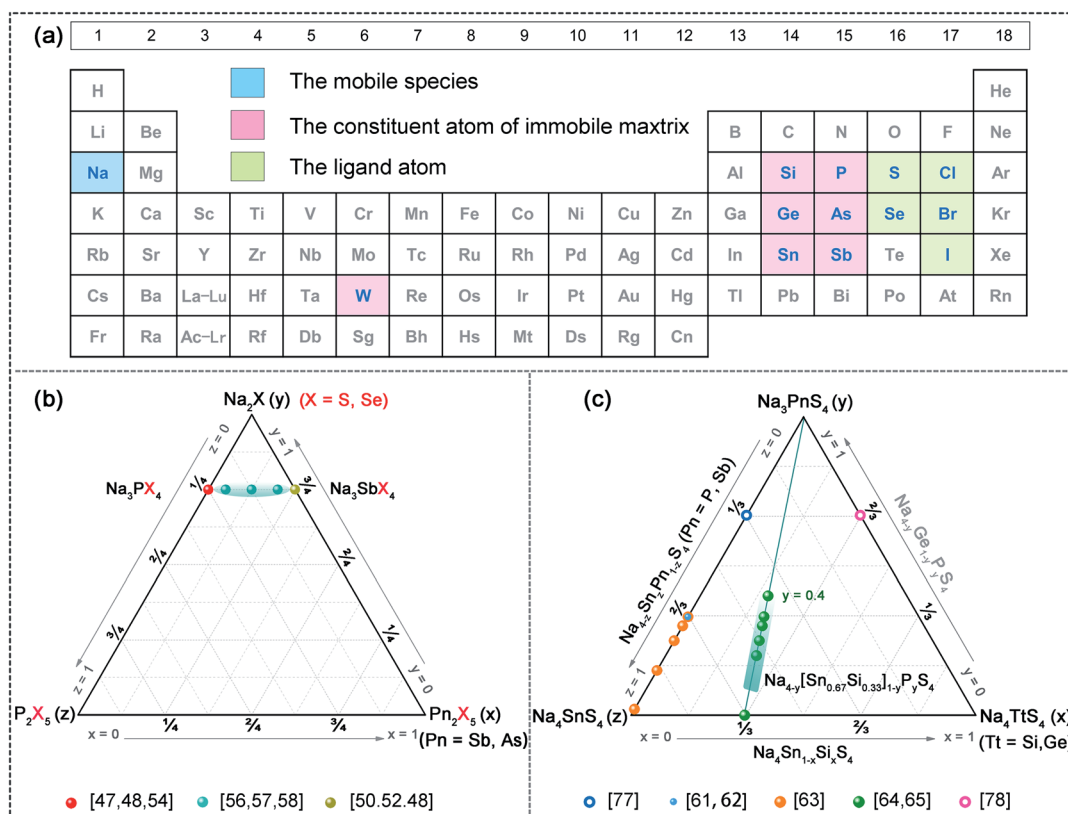

Fig. 1 (a) Periodic table of elements used for the structure building of chalcogenide-based ISSEs. The pseudo ternary phase diagram of (b) Na_3PS_4 type ISSEs and (c) $Na_{11}Sn_2PS_{12}$ type ISSEs. In (c), the samples represented by solid spheres crystallize in the space group of $I4_1/acd$, while those represented by circles are samples of impurity phase. The data are taken from ref. 47, 48, 50, 52, 54, 56–58, 61–65, 77 and 78.

5136 | J. Mater. Chem. A, 2021, 9, 5134–5148

This journal is © The Royal Society of Chemistry 2021

Table 1 The structural parameters and ion-conduction performance of the reported chalcogenide-based ISSEs

Samples	Space group (no.)	σ (S cm^{-1})	T (°C)	E_a (eV)	Ref.
t-Na$_3$PS$_4$	$P\bar{4}2_1c$ (114)	4.17×10^{-6}	50	0.40	50
c-Na$_3$PS$_4$	$I\bar{4}3m$ (217)	2.00×10^{-4}	25	0.28	51
c-Na$_3$PS$_4$	$I\bar{4}3m$ (217)	4.60×10^{-4}	25	0.20	52
94Na$_3$PS$_4$·6Na$_4$SiS$_4$	$I\bar{4}3m$ (217)	7.40×10^{-4}	—	—	75
Na$_3$PSe$_4$	$I\bar{4}3m$ (217)	1.16×10^{-3}	25	0.21	57
Na$_3$P$_{0.62}$As$_{0.38}$S$_4$	$P\bar{4}2_1c$ (114)	1.46×10^{-3}	25	0.26	60
t-Na$_3$PS$_4$	$P\bar{4}2_1c$ (114)	3.39×10^{-3}	25	0.17	76
t-Na$_{2.9375}$PS$_{3.9375}$Cl$_{0.0625}$	$P\bar{4}2_1c$ (114)	1.14×10^{-3}	30	0.25	73
Na$_{3.1}$Ti$_{0.1}$P$_{0.9}$S$_4$	—	2.30×10^{-4}	RT	0.20	77
Na$_{3.1}$Ge$_{0.1}$P$_{0.9}$S$_4$	—	2.12×10^{-4}	RT	0.21	77
Na$_{3.1}$Sn$_{0.1}$P$_{0.9}$S$_4$	—	2.50×10^{-4}	RT	0.18	77
c-Na$_{2.70}$Ca$_{0.15}$PS$_4$	$I\bar{4}3m$ (217)	0.94×10^{-3}	RT	0.49	78
t-Na$_{3.0}$PS$_{3.8}$Cl$_{0.2}$	$P\bar{4}2_1c$ (114)	1.96×10^{-3}	25	0.19	79
t-Na$_{2.9375}$SbS$_{3.9375}$Cl$_{0.0625}$	$P\bar{4}2_1c$ (114)	2.90×10^{-3}	RT	0.24	80
Na$_{2.9}$P$_{0.9}$W$_{0.1}$S$_4$	$I\bar{4}3m$ (217)	$(13 \pm 3) \times 10^{-3}$	25	—	63
t-Na$_3$SbS$_4$	$P\bar{4}2_1c$ (114)	3.00×10^{-3}	25	0.25	54
t-Na$_3$SbS$_4$	$P\bar{4}2_1c$ (114)	1.10×10^{-3}	25	0.20	53
t-Na$_3$SbS$_4$	$P\bar{4}2_1c$ (114)	1.05×10^{-3}	25	0.22	56
c-Na$_3$SbS$_4$	—	2.80×10^{-3}	RT	0.06	55
t-Na$_3$SbSe$_4$	$P\bar{4}2_1c$ (114)	3.70×10^{-3}	RT	0.19	59
Na$_{2.9}$Sb$_{0.9}$W$_{0.1}$S$_4$	$I\bar{4}3m$ (217)	$(41 \pm 8) \times 10^{-3}$	25	—	63
Na$_{2.88}$Sb$_{0.88}$W$_{0.12}$S$_4$	$I\bar{4}3m$ (217)	32×10^{-3}	25	0.18	62
Na$_{10}$SnP$_2$S$_{12}$	—	0.40×10^{-3}	25	0.36	81
Na$_{10}$GeP$_2$S$_{12}$	—	1.20×10^{-5}	RT	0.46	82
Na$_{11}$Sn$_2$PS$_{12}$	$I4_1/acd$ (142)	1.40×10^{-3}	25	0.25	64
Na$_{11}$Sn$_2$PS$_{12}$	$I4_1/acd$ (142)	$(3.7 \pm 0.3) \times 10^{-3}$	25	0.39	65
Na$_{3.75}$Sn$_{0.75}$Sb$_{0.25}$S$_4$	$I4_1/acd$ (142)	$(2-5) \times 10^{-4}$	30	—	66
Na$_{11.1}$Sn$_{2.1}$P$_{0.9}$Se$_{12}$	$I4_1/acd$ (142)	3.00×10^{-3}	25	0.30	83
Na$_{10.8}$Sn$_{1.9}$PS$_{11.8}$	$I4_1/acd$ (142)	6.70×10^{-4}	25	0.31	84
Na$_4$Sn$_{0.67}$Si$_{0.33}$S$_4$	$I4_1/acd$ (142)	1.23×10^{-5}	27	0.56	67
Na$_{3.75}$[Sn$_{0.67}$Si$_{0.33}$]$_{0.75}$P$_{0.25}$S$_4$	$I4_1/acd$ (142)	1.61×10^{-3}	27	0.26	67
Na$_{3.67}$[Sn$_{0.67}$Si$_{0.33}$]$_{0.67}$P$_{0.33}$S$_4$	$I4_1/acd$ (142)	6.55×10^{-4}	27	0.30	67
Na$_{3.6}$[Sn$_{0.67}$Si$_{0.33}$]$_{0.6}$P$_{0.4}$S$_4$	$I4_1/acd$ (142)	5.00×10^{-4}	27	0.31	67
Na$_{3.8}$[Sn$_{0.67}$Si$_{0.33}$]$_{0.8}$Sb$_{0.2}$S$_4$	$I4_1/acd$ (142)	1.75×10^{-4}	26	0.31	69
Na$_{3.57}$[Sn$_{0.67}$Si$_{0.33}$]$_{0.67}$P$_{0.33}$S$_{3.9}$Cl$_{0.1}$	$I4_1/acd$ (142)	9.40×10^{-4}	27	0.28	68
Na$_{3.57}$[Sn$_{0.67}$Si$_{0.33}$]$_{0.67}$P$_{0.33}$S$_{3.9}$Br$_{0.1}$	$I4_1/acd$ (142)	9.20×10^{-4}	27	0.28	68
Na$_{3.57}$[Sn$_{0.67}$Si$_{0.33}$]$_{0.67}$P$_{0.33}$S$_{3.9}$I$_{0.1}$	$I4_1/acd$ (142)	1.08×10^{-3}	27	0.24	68

conductivity.[55,76] The operation of the solid phase method is simple and the composition of the product is easily controlled, while the particle size is generally large. However, when the as-prepared samples are applied in all solid-state batteries, poor contact in the composite electrode exists owing to insufficient physical mixing of SEs and cathode materials. Thus the liquid-phase method is developed to prepare ISSEs, in which a homogeneous powder can be obtained after the wet chemistry process. What's more, SE coated cathode materials can be afforded. As a result, the liquid-phase method is widely used to synthesize chalcogenide-based ISSEs.[78–82] Up to now, Na$_3$PS$_4$, Na$_3$SbS$_4$, Na$_{4-x}$Sn$_{1-x}$Sb$_x$S$_4$, Na$_{3-x}$Sb$_{1-x}$W$_x$S$_4$ and Na$_{3-x}$PS$_{4-x}$Cl$_x$ have been successfully synthesized through the liquid-phase method.[53,86–88]

Two typical liquid-phase approaches, the "liquid-phase reaction" and the "solution-process" were successfully applied to prepare chalcogenide-based SEs.[53,86–88] For the "liquid-phase reaction", as shown in the above part of Fig. 2b, precursors are fully dissolved in an appropriate solvent. After the reaction, ISSEs are obtained by the following precipitation and heat treatment process. In 2015, c-Na$_3$PS$_4$ was firstly synthesized *via*

a liquid-phase reaction by Yubuchi *et al.*[89] The precursors of Na$_2$S and P$_2$S$_5$ with a molar ratio of 3 : 1 were added in *N*-methylformamide (NMF) solvent. Pure c-Na$_3$PS$_4$ with a room temperature ionic conductivity of 2.6×10^{-6} S cm^{-1} was obtained following precipitation and heat treatment processes.[89] Kim *et al.* successfully prepared Na$_{3-x}$Sn$_{1-x}$Sb$_x$S$_4$ (x = 1, 0.25) with an aqueous-solution synthesis route and coated the positive electrode FeS$_2$ using the same strategy (Fig. 2d).[87] The "solution-process" is conducted by adding the as-prepared SEs in a suitable solvent, which is beneficial for coating SEs. However this method relies on conventional synthetic protocols to prepare pure SEs. In which, the as-prepared SEs were dissolved in a suitable solvent, followed by evaporation and heat treatment processes.[53] Banerjee *et al.* prepared t-Na$_3$SbS$_4$ with a room temperature ionic conductivity of 1.1×10^{-3} S cm^{-1}. Then the "solution-process" was applied and Na$_3$SbS$_4$ with room temperature ionic conductivities of 2.3×10^{-4} S cm^{-1} and 2.6×10^{-4} S cm^{-1} was obtained using MeOH or H$_2$O as the solvent, respectively. What's more, as shown in Fig. 2c, Na$_3$SbS$_4$ is successfully coated on the surface of the positive electrode

This journal is © The Royal Society of Chemistry 2021

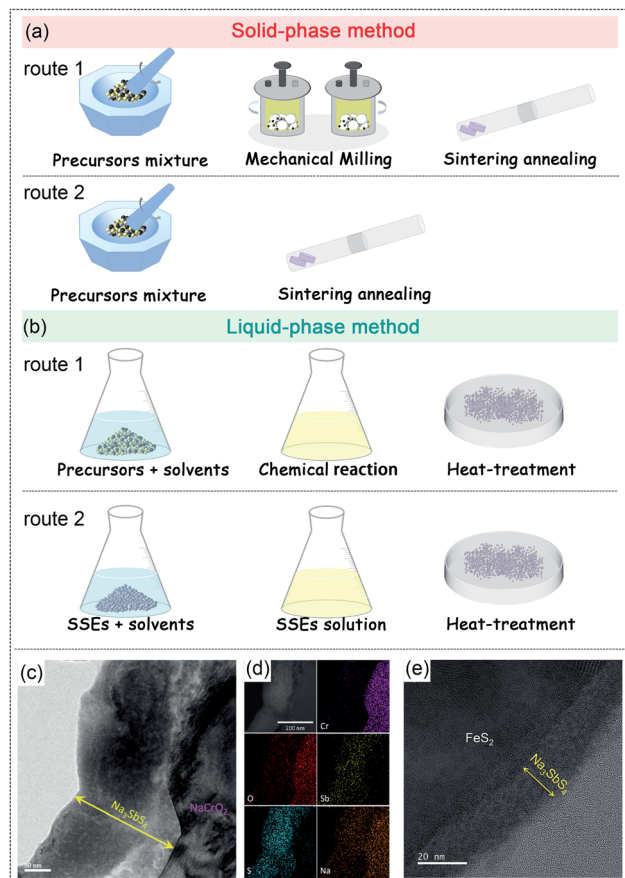*J. Mater. Chem. A*, 2021, **9**, 5134–5148 | **5137**

Fig. 2 (a) Schematic of the synthetic routes for chalcogenide-based ISSEs of the solid-phase method, (b) the liquid-phase method, in detail, above is the "liquid-phase reaction" and below is the "solution-process", respectively. (c) HRTEM images of the FIB-cross-sectioned Na_3SbS_4-coated $NaCrO_2$; (d) annular dark-field (ADF) TEM image of FIB-sectioned Na_3SbS_4-coated NCO and its corresponding EDXS elemental maps.[53] Reproduced with permission from ref. 53. Copyright (2016), Wiley. (e) HRTEM images of the FIB-cross-sectioned Na_3SbS_4-coated FeS_2.[87] Reproduced with permission from ref. 87. Copyright (2018), The Royal Society of Chemistry.

$NaCrO_2$ through the "solution-process". The ionic conductivities of chalcogenide-based ISSEs obtained from the liquid-phase methods vary in a wide range, and are generally lower in contrast to those obtained from the solid-phase method, likely related to the impurity phase, off-stoichiometry and crystallinity.[53,62,86–88,90] Nevertheless, the wet chemistry process is vital to forming a solid electrolyte coating layer on the electrode particles with improved electrochemical performances.[53,87] The capacity and cycle stability are improved due to the enhanced ionic conductivity of Na^+, which allows better transportation across the electrode/electrolyte interface.[91]

4. Structural design of chalcogenide-based ISSEs

4.1 Na_3PS_4 type ISSEs

4.1.1 Crystal structure of Na_3PS_4.
As shown in Fig. 3a and b, the Na_3PS_4 type ISSEs hold two kinds of crystalline phases, in

which the cubic phase (c-) belongs to the $I\bar{4}3m$ space group with lattice parameter $a = 6.9965$ Å and the tetragonal phase (t-) belongs to the $P\bar{4}2_1c$ space group with lattice parameters of $a = 6.9520$ Å and $c = 7.0757$ Å.[50,75] t-Na_3PS_4 is a room temperature phase and c-Na_3PS_4 is a high temperature phase.[50,51] The distinction between these two phases is tiny, which just exists in the lattice parameters of 1.1% and lattice volume of 0.2%, respectively.[92] In the cubic phase, the $[PS_4]$ polyhedra are arranged in a body centered cubic (bcc) lattice to construct the rigid matrix and Na^+ occupies the Na(6b) site. And Tanibata *et al.* proposed the additional interstitial Na(12d) site.[75] As for the tetragonal phase, the Na(6b) site splits into two sites of Na(2a) and Na(4d), because of a minor rotation of the $[PS_4]$ polyhedra. However, the MD simulations results (Fig. 3c and d) reveal that the slight difference barely influences the Na-ion distributions.[92] The local scale of the structures for both phases is similar, which has been confirmed by means of synchrotron pair distribution function (PDF) analyses (Fig. 3e).[93] c- and t-Na_3PS_4 show similar Na^+ ion conductivities on the microscopic level and different Na^+ ion diffusion behaviors in the local scale, the latter being influenced by the concentration of Na^+ ion defects.[92] Because of similar structural parameters, the two structures can be converted to each other by element doping,[63,78,92–94] which will be carefully discussed in Section 4.1.3. Very recently, Famprikis *et al.* studied the synthesis–property relationships affected by mechanochemistry. Taking Na_3PS_4 as an example, they found that mechanochemistry could induce phase transition, and stabilize the cubic phase, as well as affect ion transport.[95]

4.1.2 Isovalent substitution in Na_3PS_4 type ISSEs.
Increasing the size of the constituent atoms of the skeleton structure can expand the ionic transport channel, and enhance the ionic conductivity of chalcogenide-based solid electrolytes.[53,54,56,57,59] Replacing S with Se in c-Na_3PS_4 leads to Na_3PSe_4 solid electrolytes with improved ionic conductivity (4.6×10^{-4} S cm^{-1} *vs.* 1.16×10^{-3} S cm^{-1} at room temperature).[57,96] Krauskopf *et al.* studied the lattice dynamics of the $Na_3PS_{4-x}Se_x$ system by means of Raman spectroscopy, inelastic neutron scattering, phonon measurements, and density functional theory calculations. They found that the substitution of Se for S not only affected the chemical environment of the skeleton structure, but also reduced the symmetry of the $[PS_4]^{3-}$ tetrahedron. The migration barrier and the pre-indicative factors were induced as the lattice softened, and therefore Se substitution could accelerate Na^+ ion transport.

The replacement of P with Sb in Na_3PnS_4 (Pn = P, Sb) can also enhance Na^+ ion mobility.[53,54,56] Moreover, the resultant Na_3SbS_4 shows better air stability than Na_3PS_4 supported by "the theory of soft and hard acids and bases".[56] Isovalent substitution does not change the Na^+ ion concentrations in the structure of Na_3PS_4. However, the larger atom leads to an enlarged crystal volume, yielding an increased Na^+ ion mobility in the structure due to the "size effect", as shown in Fig. 4a.[59] It should be mentioned that the "size effect" is not always monotonous. Yu *et al.* introduced arsenic in Na_3PS_4 to form a solid solution structure $Na_3P_{1-x}As_xS_4$. The introduction of arsenic not only expands the ionic transport channel due to the
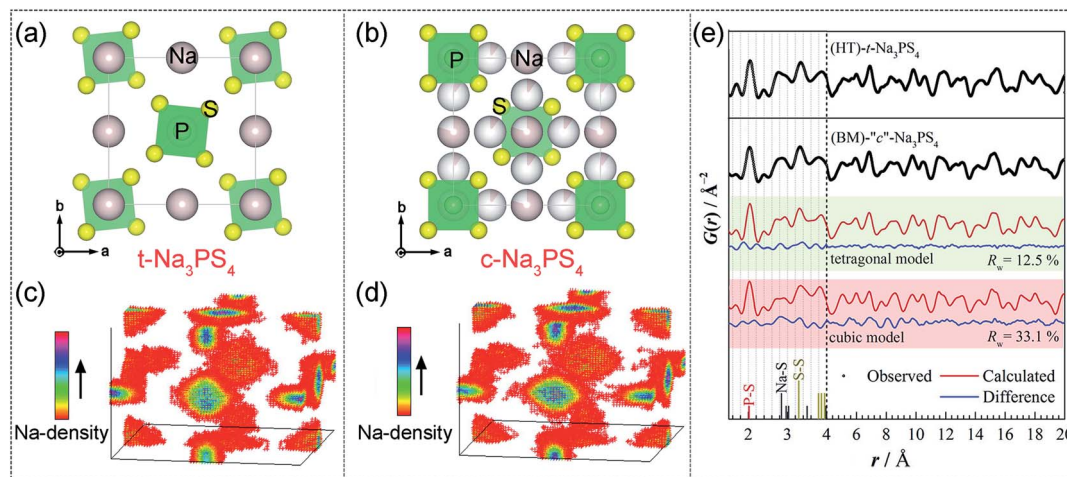
5138 | *J. Mater. Chem. A*, 2021, **9**, 5134–5148

This journal is © The Royal Society of Chemistry 2021

Fig. 3 The crystal structure of (a) t-Na_3PS_4 and (b) c-Na_3PS_4. These figures are drawn according to the crystal structure parameters reported in ref. 50 and 75, respectively; the Na-distribution during a 100 ps. MD simulation at 525 K for (c) t-Na_3PS_4 and (d) c-Na_3PS_4.[92] Reproduced with permission from ref. 92. Copyright (2016), American Chemical Society. (e) Experimentally obtained $G(r)$ data and fitting results for t-Na_3PS_4 and c-Na_3PS_4.[93] Reproduced with permission from ref. 93. Copyright (2018), American Chemical Society.
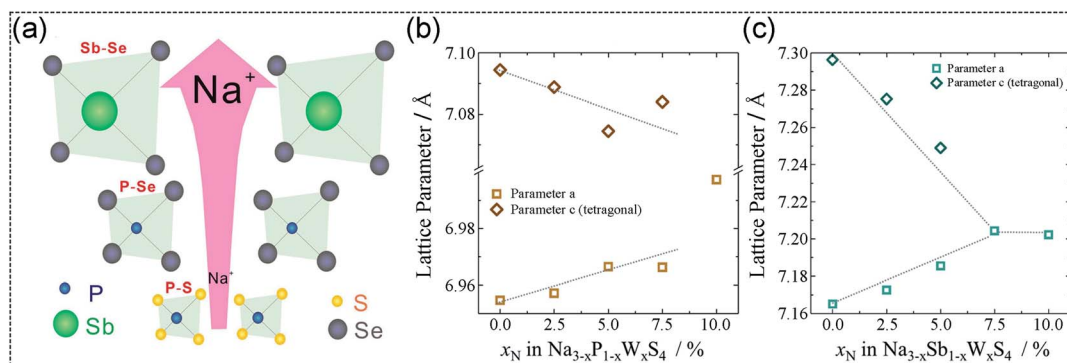
Fig. 4 (a) Schematic diagram of Na^+ ion diffusion in different compounds.[59] Refined lattice parameters of (b) $Na_{3-x}P_{1-x}W_xSb_4$ and (c) $Na_{3-x}Sb_{1-x}W_xS_4$ as a function of composition, showing the structural changes during substitution.[63] Reproduced with permission from ref. 63. Copyright (2019), American Chemical Society.

larger atomic radius, but also affects the chemical environment and bonding parameter in the structure. As a result, $Na_3P_{0.62}As_{0.38}S_4$ with the highest room-temperature ionic conductivity (1.46×10^{-3} S cm^{-1}) is obtained when 38 percent of P is replaced by As in the composition.[60]

4.1.3 Aliovalent doping in Na_3PS_4 type ISSEs. Aliovalent doping based on the Na_3PS_4 structure can create point defects such as Na^+ ion vacancies or interstitial sites, thereby enhancing ion conductivity.[92,94] Both theoretical simulations and multiple characterization methods have been applied to unravel the aliovalent doping effect on Na^+ ion dynamics in Na_3PS_4 and its analogs. In 2014, Tanibata *et al.* introduced Si in c-Na_3PS_4 and obtained 94Na_3PS_4·6Na_4SiS_4 with an optimal ionic conductivity of 7.4×10^{-4} S cm^{-1} at room temperature, which was 1.7 times higher than that of bare Na_3PS_4.[75] Subsequently, theoretical calculations showed that the ionic conductivity of c-Na_3PS_4 with the exact stoichiometric ratio was actually very low, similar to the that of the tetragonal phase.[94] Aliovalent cation (Sn^{4+}, Si^{4+}, and Ge^{4+}) doping in c-Na_3PS_4 created Na^+ ion interstitial sites,

which was helpful for Na^+ diffusion, yielding a higher Na^+ ion conductivity. Theoretical simulations show that the room temperature ionic conductivity of the 6.25% Si-doped sample was 1.66×10^{-3} S cm^{-1}, which is close to the experimental value reported previously. Unlike the Si-doped case, Sn and Ge doping can not only increase the number of Na interstitial sites, but also broaden the Na^+ ion diffusion channels. By tailoring the doping amount of Sn in the structure, an optimal composition for a 6.25% Sn doped sample was obtained and delivered an ultrafast room temperature ionic conductivity up to 1.07×10^{-2} S cm^{-1}. Rao *et al.* studied the effect of Ge^{4+}, Ti^{4+}, and Sn^{4+} doping on the ion conductivity of Na_3PS_4 type and found that the Sn^{4+} doped sample, $Na_{3.1}Sn_{0.1}P_{0.9}S_4$, showed the highest ionic conductivity among these different compositions and excellent solid-state sodium battery performance.[77] Moon *et al.* developed Ca-doped Na_3PS_4 ($Na_{3-2x}Ca_xPS_4$ ($0 < x \le 0.375$)), in which the maximum ionic conductivity reached about 1 mS cm^{-1} at room temperature.[78] Applying Ca doping on t-Na_3PS_4, partial Na^+ was substituted by Ca^{2+}, leading to the

This journal is © The Royal Society of Chemistry 2021

J. Mater. Chem. A, 2021, **9**, 5134–5148 | **5139**

formation of Na^+ vacancies and tetragonal-to-cubic phase transition. In 2016, Klerk *et al.* studied the role of Na^+ vacancies in ionic transport in Na_3PS_4. Their results show that in theory 2% Na^+ vacancies can enhance the ionic conductivity by an order of magnitude and halogen doping is an effective approach to introduce vacancies in the structure.[92] Later, Chu *et al.* successfully synthesized Cl-doped t-Na_3PS_4 and found the obtained optimal composition t-$Na_{2.9375}PS_{3.9375}Cl_{0.0625}$ with improved ionic conductivity and electrochemical stability.[73]

More recently, Hayashi *et al.* introduced W^{6+} in the structure of Na_3SbS_4 for the first time and found that the optimal composition, $Na_{2.88}Sb_{0.88}W_{0.12}S_4$, showed a record high ionic conductivity (3.2×10^{-2} S cm^{-1} at room temperature) and excellent air stability. The obtained ionic conductivity was not only higher than that of all of those reported chalcogenide-based Na electrolytes, but also higher than that of current organic liquid electrolytes, showing great potential as solid electrolytes for all-solid-state batteries.[62] Subsequently, Fuchs *et al.* used the same strategy of W doping for the Na_3PnS_4 (Pn = P, Sb) system to systematically reveal the structure–property relationship.[63] They prepared a series of solid solutions formulated as $Na_{3-x}Pn_{1-x}W_xS_4$ (Pn = P, Sb) and found that the degree of distortion of $[MS_4]$ tetrahedron in the tetragonal phase structure became smaller as a function of the increasing W amount in the structure. As shown in Fig. 4b and c, when $x = 0.1$, the phase of these doped samples transferred from tetragonal to cubic and the optimal composition c-$Na_{2.9}P_{0.9}W_{0.1}S_4$ is obtained with a ultra-high room temperature ionic conductivity (($1.3 \pm 0.3) \times 10^{-2}$ S cm^{-1}). For the W-doped Na_3SbS_4, the highest ion conductivity is ($4.1 \pm 0.8) \times 10^{-2}$ S cm^{-1} for $Na_{2.9}Sb_{0.9}W_{0.1}S_4$, which is almost 3 times higher than that of c-$Na_{2.9}P_{0.9}W_{0.1}S_4$ and may be associated with the much larger atomic radius of Sb than P.[62,63]

4.2 $Na_{11}Sn_2PS_{12}$ type ISSEs

Besides the Na_3PS_4 type ISSEs, an important family of chalcogenide-based sodium solid electrolytes is the $Na_{11}Sn_2PS_{12}$ type with a space group of $I4_1/acd$, delivering high room temperature ionic conductivities at the order of 10^{-3} S cm^{-1}.[64,65] In 2011, a new type of Li ion conductor $Li_{10}GeP_2S_{12}$ (LGPS) with a high room temperature ion conductivity (1.2×10^{-2} S cm^{-1}) was reported, even comparable to current organic liquid electrolytes.[97] The Na^+ ion shows slightly larger ionic radii than Li^+ (116 pm *vs.* 90 pm), providing the possibility of replacing Li^+ with Na^+ in the $Li_{10}GeP_2S_{12}$ structure. In 2015, Kandagal *et al.* predicted the existence of $Na_{10}GeP_2S_{12}$ with a space group of $P4_2/nmc$ (in consist with the LGPS) by the theoretical method.[98] Later, Richards *et al.* generalized it to the $Na_{10}MP_2S_{12}$ (M = Si, Ge, Sn) system.[81] However, the as-prepared $Na_{10}SnP_2S_{12}$ and $Na_{10}GeP_2S_{12}$ show totally different diffraction peaks from $Li_{10}GeP_2S_{12}$. The XRD results show that the diffraction pattern of the as-prepared samples consist of diffraction peaks indexed to mixed phases including P_2S_5, Na_2S_5, Na_3PS_4 and an unknown phase.[81,82]

4.2.1 $Na_{11}Sn_2PnCh_{12}$ (Pn = P, Sb; Ch = S, Se) system. A new phase formulated as $Na_{11}Sn_2PS_{12}$ was firstly reported by

tailoring the Sn/P ratio from 2 : 1 to 1 : 2 in the structure of $Na_{10}SnP_2S_{12}$. This new phase showed a different space group ($I4_1/acd$) compared with $Na_{10}MP_2S_{12}$ (M = Si, Ge, Sn) and high room temperature ion conductivities, 1.4×10^{-3} S cm^{-1} for the cold-pressed sample and 3.7×10^{-3} S cm^{-1} for the annealed sample, respectively.[64,65]

(1) *Crystal structure.* The crystal structure of $Na_{11}Sn_2PS_{12}$ is illustrated in Fig. 5a. It has a tetragonal phase structure with a space group of $I4_1/acd$. In this structure, Sn and P form a tetrahedron with S, and then stack to construct the rigid matrix with Na^+ ions distributed over six different Na sites.[64] Na(1) to Na(5) are distributed in a varied irregular NaS$_6$ octahedron in the structure, while Na(6) is located at an interstitial site.[64,99,101] A three-dimensional Na^+ ion diffusion channel is observed in the structure of $Na_{11}Sn_2PS_{12}$ based on the network of different kinds of Na sites. Richards *et al.* investigated the Na^+ ion migration path of $Na_{11}Sn_2PS_{12}$ with a combination of single-crystal diffraction analysis and AIMD simulations (see Fig. 5b–e). The Na^+ ions migrate along the path of the Na(4)–Na(1)–Na(3)–Na(1) chains in the *c* axis. In the *ab* plane, the Na^+ ions migrate along the paths of Na(4)–Na(2)–Na(4) or Na(3)–Na(2)–Na(3) at $z = 0$, and paths of Na(5)–Na(1)–Na(5) at $z = 0.875$, while Na(6) takes part as an parking site connecting Na(1) and Na(2) in the structure.[64,99]

(2) *Substitution.* Duchardt *et al.* obtained a new kind of ISSE with the composition of $Na_{11.1}Sn_{2.1}P_{0.9}Se_{12}$ by replacing S in $Na_{11}Sn_2PS_{12}$ with Se.[83] The as-prepared Se-based ISSEs show similar room temperature ionic conductivities (3.0×10^{-3} S cm^{-1} *vs.* 3.7×10^{-3} S cm^{-1}) but lower activation energies (0.39 eV *vs.* 0.30 eV) compared to $Na_{11}Sn_2PS_{12}$. The lower activation energy is ascribed to the softer crystal lattice of the Se-based sample. Heo *et al.* synthesized a series of $Na_{4-x}Sn_{1-x}Sb_xS_4$ ($0.02 \leq x \leq 0.33$) solid solution structures and found that $Na_{3.75}Sn_{0.75}Sb_{0.25}S_4$ with a space group of $I4_1/acd$ delivered the highest room temperature ionic conductivity of ($2–5) \times 10^{-4}$ S cm^{-1}. Both Sb and Sn belong to the "soft acid" and S belongs to the "soft base", so that the good compatibility between these two based on "soft and hard acid–base theory" yields excellent air stability for these electrolytes.[66] Ramos *et al.* compared the correlation of Na^+ ion transport in the $Na_{11}Sn_2PnS_{12}$ (Pn = P, Sb) system and found that $Na_{11}Sn_2SbS_{12}$ exhibited slower ion mobility among these samples due to the stronger Na^+–S^{2-} coulombic attractions.[99] In addition, Zhang *et al.* further analyzed the kinetics of the anion–cation coupling in a $Na_{11}Sn_2PnX_{12}$ (Pn = P, Sb; X = S, Se) superionic conductor system through quasi-elastic neutron scattering. They found that the $[PS_4]^{3-}$ polyanion could rotate rapidly at room temperature in the P based system due to the "paddle-wheel mechanism", while a similar phenomenon was not observed for the SbS_4^{3-} polyanion (Fig. 5f and g). This kind of rotational coupling can widen the "bottleneck" in the progress of Na^+ ion motion, yielding higher Na^+ ion conductivity in the P-based structure($[PX_4](X = S, Se)$).[100] Kraft *et al.* reported that the decreasing Na^+ pathway size led to increased activation energies in the Sb substituted $Na_{11}Sn_2PS_{12}$ system ($Na_{11+x}Sn_{2+x}(Sb_{1-y}P_y)_{1-x}S_{12}$).[102]

5140 | *J. Mater. Chem. A*, 2021, **9**, 5134–5148
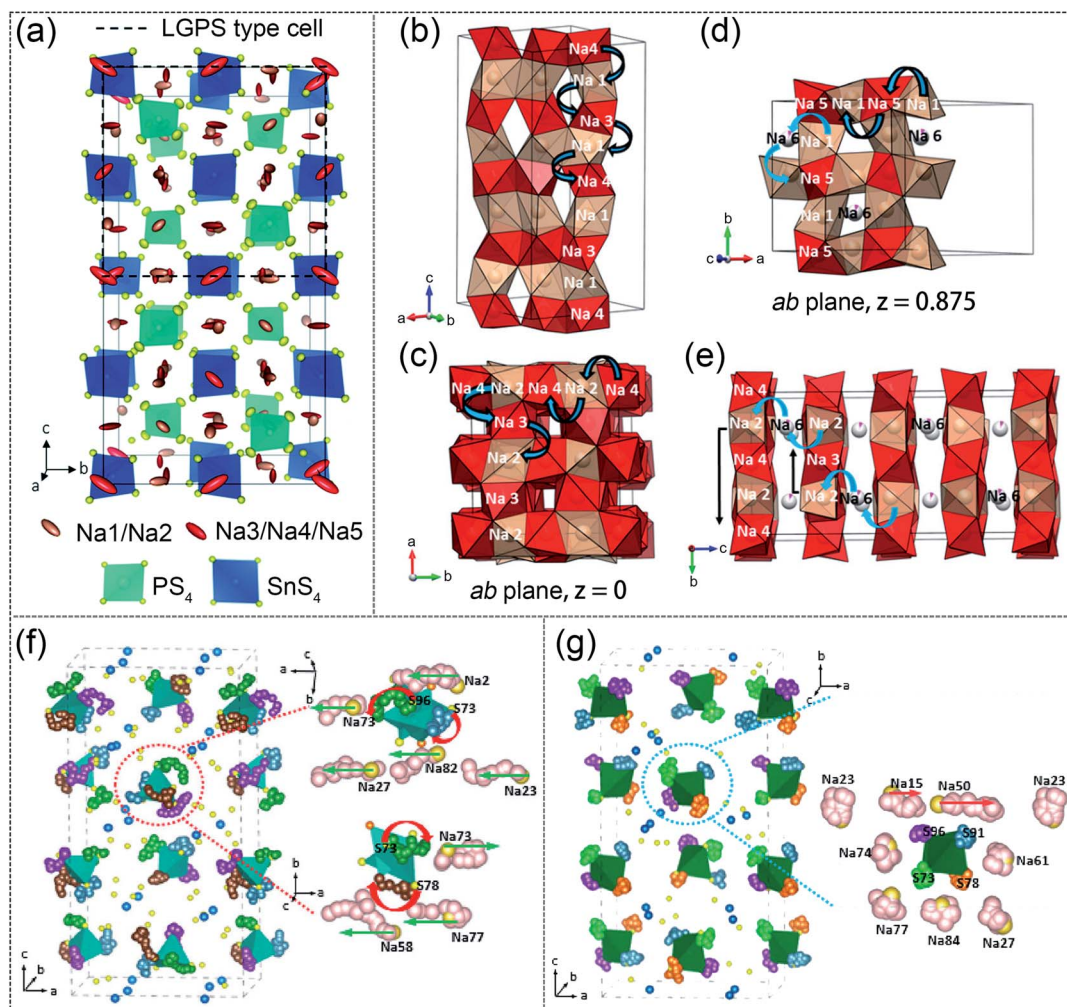
This journal is © The Royal Society of Chemistry 2021

Fig. 5 (a) Structure of $Na_{11}Sn_2PS_{12}$ from single crystal data.[64] Reproduced with permission from ref. 64. Copyright (2018), The Royal Society of Chemistry. (b) View of the diffusion channels interconnecting Na(4)–Na(3)–Na(1) sites along the c axis. (c) View of the chains in the ab plane formed by Na(4)–Na(2)–Na(4) or Na(3)–Na(2)–Na(3) at $z = 0$. (d) Interconnection points created by the Na(6) site between the diffusion channels formed by Na(1)–Na(5)–Na(1) chains at $z = 0.875$. (e) View of the interconnection points created by the Na(6) site along the c axis between the diffusion channels that run along the ab plane (composed of Na(4)–Na(2)–Na(4) or Na(3)–Na(2)–Na(3)).[99] Reproduced with permission from ref. 99. Copyright (2018), American Chemical Society. (f) The trajectories of the S ligands of $[PS_4]^{3-}$ polyanions in $[Na_{11}Sn_2]PS_{12}$ between 21 and 22 ps from AIMD simulation at 1050 K, (g) The trajectories of the S ligands of $[SbS_4]^{3-}$ polyanions in $[Na_{11}Sn_2]SbS_{12}$ between 21 and 22 ps from AIMD simulation at 1050 K.[100] Reproduced with permission from ref. 100. Copyright (2019), American Chemical Society.

4.2.2 $Na_{12-x-y}[Sn_2Si]_{1-x}Pn_xS_{12-y}X_y$ (Pn = P, Sb; X = Cl, Br, I) ($0 \leq x \leq 0.6$; $y = 0$, 0.1) system. Recently, our group reported a unique ISSE, $Na_4Sn_{0.67}Si_{0.33}S_4$ (space group: $I4_1/acd$ (no. 142)), showing an isostructural structure with $Na_{11}Sn_2PS_{12}$ but a higher Na^+ ion concentration.[67] A series of solid solutions with the formulation of $Na_{4-x}[Sn_{0.67}Si_{0.33}]_{1-x}P_xS_4$ ($0 \leq x < 0.6$) were obtained by the partial substitution of $[Sn_{0.67}Si_{0.33}]$ with P in the $Na_4Sn_{0.67}Si_{0.33}S_4$ structure. P substitution in the structure not only increases the number of vacancies but also weakens the Na–S interaction, thus improving the Na^+ ion conductivity. The optimal composition was found with the highest ionic conductivity of 1.6×10^{-3} S cm^{-1} when $x = 0.25$. A similar strategy has also been performed to replace part of $[Sn_{0.67}Si_{0.33}]$ with Sb and found that the introduction of Sb could also enhance the Na^+ ion conductivity, while this incremental effect was not as good as that of the P-substituted samples.

In this system, from Na_4SnS_4 to $Na_4Sn_{0.67}Si_{0.33}S_4$, the Na^+ ion conductivity of the latter was improved by 3 orders of magnitude, mainly due to the change of the crystal structure (Fig. 6a). When one third of Sn was replaced by Si, the crystal structure changes from $P\bar{4}2_1c$ to $I4_1/acd$, and thus the 3D channels for Na^+ ion migration were formed. For $Na_4Sn_{0.67}Si_{0.33}S_4$, the Na^+ sites from Na(1) to Na(5) are highly occupied, so that the ionic conductivity at room temperature is extremely low (1.23×10^{-5} S cm^{-1}). However, the substitution of P or Sb for $[Sn_{0.67}Si_{0.33}]$ can effectively increase the Na^+ vacancy concentration, therefore significantly enhancing the ionic conductivity.[68,69]

Furthermore, the strategy of halogen doping was successful achieved in this system. Using $Na_{3.67}[Sn_{0.67}Si_{0.33}]_{0.67}P_{0.33}S_4$ as the pristine structure, the halogen-doped samples $Na_{3.57}[Sn_{0.67}Si_{0.33}]_{0.67}P_{0.33}S_{3.9}X_{0.1}$ (X = Cl, Br, I) were successfully

This journal is © The Royal Society of Chemistry 2021
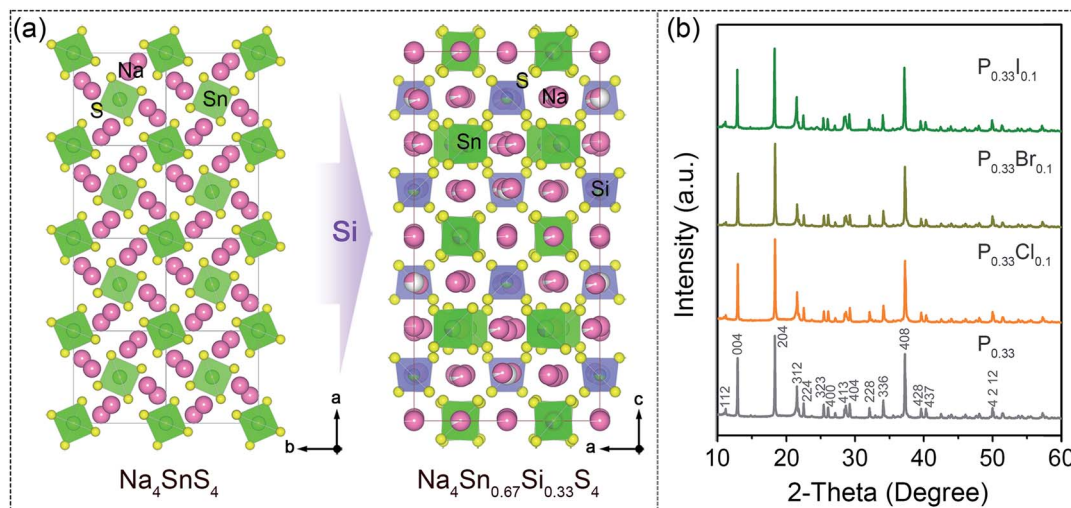
J. Mater. Chem. A, 2021, **9**, 5134–5148 | **5141**

Fig. 6 (a) Crystal structure of Na_4SnS_4 with a $4 \times 2 \times 1$ supercell on the left and $Na_4Sn_{0.67}Si_{0.33}S_4$ with a $1 \times 1 \times 1$ supercell on the right. Na_4SnS_4 and $Na_4Sn_{0.67}Si_{0.33}S_4$ belong to space groups of $P\bar{4}2_1c$ and $I4_1/acd$, respectively. (b) XRD patterns of the samples formulated as $Na_{3.67-y}[Sn_{0.67}Si_{0.33}]_{0.67}P_{0.33}S_{4-y}X_y$, in which X = Cl, Br, and I; y = 0, 0.1, respectively. All XRD patterns were indexed to the space group of $I4_1/acd$ (142).[68] Reproduced with permission from ref. 68. Copyright (2020), American Chemical Society.

synthesized.[68] The XRD patterns in Fig. 6b revealed that no impurity existed in the system. Besides increasing the number of Na^+ ion vacancies, halogen doping lowers the Na^+ ion migration barrier on account of the high polarizability of halogen atoms. The I-doped sample $Na_{3.57}[Sn_{0.67}Si_{0.33}]_{0.67}$-$P_{0.33}S_{3.9}I_{0.1}$ delivers the highest ambient ionic conductivity (1.08×10^{-3} S cm^{-1}) and the lowest activation energy (0.24 eV) among all of these doped samples. What's more, the strategy of halogen doping was successfully demonstrated on ISSEs crystallizing in the space group of $I4_1/acd$ for the first time. From the above results, $Na_4Sn_{0.67}Si_{0.33}S_4$ can be taken as a high tolerance structural template for extensive chemical manipulation.

5. Structure–activity relationships

5.1 Sodium ionic transport

In crystalline–polycrystalline SE systems, the connected ionic channel in the crystal structure is the prerequisite for fast ionic transport. Toward this end, the transport of ions can be adjusted by changing the size of the ionic pathway, the lattice volume, the bottleneck, the concentration of defects (vacancy or interstitial), the polarizability of ligand atoms, and other structural parameters.[71,72] The following discussion is included with respect to the Na_3PS_4 type ($Na_{3-y}P_{1-x}Pn_xW_yCh_4$ (Pn = Sb, As; Ch = S, Se)) and the $Na_{11}Sn_2PS_{12}$ type ($Na_{11}Sn_2PnCh_{12}$ and $Na_{12-x-y}[Sn_2Si]_{1-x}Pn_xS_{12-y}X_y$ (Pn = P, Sb; X = Cl, Br, I)) ISSEs.

(1) According to the description in Section 3.1, for the Na_3PS_4 type ISSEs, the factors influencing the ionic conductivity are relatively simple. The crystal structure of cubic Na_3PS_4 and tetragonal Na_3PS_4 is very similar. The vacancy or interstitial defects greatly affect the ionic conductivity.[92,94] Besides, the effect of the lattice volume on ionic diffusion is more obvious. Either replacing S with Se or replacing P with Sb, the ionic conductivities are significantly enhanced due to the larger ion

radii of the doped elements.[57,59] In addition, due to the high polarizability of Se, the introduction of Se into the structure can also soften the crystal lattice, thereby reducing the activation energy and the pre-factor of ionic migration.[103,104]

(2) In contrast, the factors influencing the ionic conductivity of $Na_{11}Sn_2PS_{12}$ type ISSEs are more complicated. For example, from $Na_{11}Sn_2PS_{12}$ to $Na_{11.1}Sn_{2.1}P_{0.9}Se_{12}$, the change of the coordination atom from S to Se (with a larger radius) mainly reduces the activation energy, but only slightly influences the ionic conductivity.[83] As for $Na_{11}Sn_2PS_{12}$ and $Na_{11}Sn_2SbS_{12}$, after replacing P with Sb, the ionic conductivity decreases obviously. The possible explanation is that Sb has a larger atomic radius, and the introduction of Sb also brings greater steric hindrance; hence the replacement is not conducive to the mobility of Na^+ ions.[99] In addition, the kinetic analysis of the anion–cation coupling in the $Na_{11}Sn_2PnX_{12}$ (Pn = P, Sb; X = S, Se) system indicates the existence of the "paddle-wheel mechanism" in P-based samples, which is also beneficial for Na^+ ion diffusion.[100]

(3) For $Na_{12}Sn_2SiS_{12}$, although it is isostructural with Na_{12}-Sn_2PS_{12}, its structure tolerance is higher. It is the first time to find ISSEs with a rigid matrix only constructed by group 14 elements (Sn and Si). What's more, it can be used as a template structure for wide chemical manipulation.[67–69] Thus the Na^+ ion concentration in the structure can be controlled flexibly by both cation substitution and anion doping, which provides a good structural template for the study of fundamental issues in this type of ISSE.

(4) The ionic conductivities and activation energies of the main chalcogenide-based ISSEs are concluded in Fig. 7. Therein, the W^{6+} doped Na_3PnS_4 shows the highest ionic conductivity,[62,63] which can reach above 10^{-2} S cm^{-1}. Except for that, most of the ion conductivities fall between the values of $(0.2–4) \times 10^{-3}$ S cm^{-1}, and the activation energies are between 0.2 and 0.3 eV. Among them, the activation energies of Na_3PnS_4
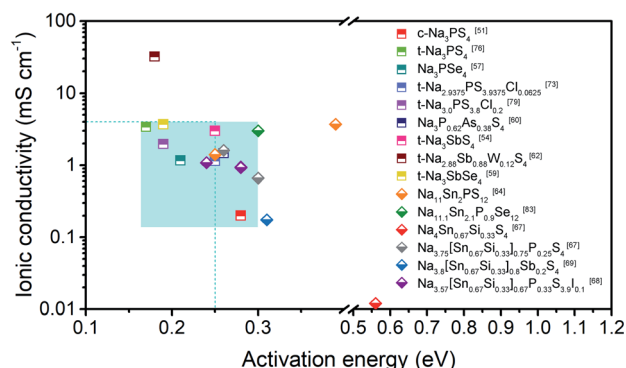
Fig. 7 The ionic conductivity and activation energy relationship diagram of the reported chalcogenide-based ISSEs. Therein, the half up square symbol represents the ISSEs formulated as $Na_{3-y}P_{1-x}Pn_x$-W_yCh_4 (Pn = Sb, As; Ch = S, Se), and the half down diamond symbol represents the ISSEs formulated as $Na_{11}Sn_2PnCh_{12}$ and $Na_{12-x-y}[Sn_2Si]_{1-x}Pn_xS_{12-y}X_y$ (Pn = P, Sb; X = Cl, Br, I). The data are taken from ref. 51, 54, 57, 59, 60, 62, 64, 67–69, 73, 76, 79 and 83.

type ISSEs are generally lower. Most of them are less than 0.25 eV, while the values for $Na_{11}Sn_2PS_{12}$ type ISSEs are generally greater than 0.25 eV. In addition, the electronic conductivities for most reported sulfide-based ISSEs are below the level of 10^{-9} S cm^{-1}, which are far lower than their ionic conductivities.[54,63]

5.2 Structural correlations in the two kinds of ISSEs

Duchardt et al. pointed out that the Na$^+$ positions were arranged similarly in the $Na_{11}Sn_2PS_{12}$ and Na_3PS_4 structures.[65] As shown in Fig. 8a and b, the arrangements of Na$^+$ positions in both

structures are analogous to the NbO topology, an ordered deficient NaCl-type structure. On the consideration of a 2 × 1 × 1 NaCl supercell with 16 atoms, 12 of them are occupied in the NbO type structure and 4 vacancies remain. In the structure of Na_3PS_4 ($Na_{12}[PS_4]_4$), all vacancies of the NbO type structure are full with the $[PS_4]^{3-}$ tetrahedron (Fig. 8a). In terms of $Na_{11}Sn_2$-PS_{12} ($Na_{11}[SnS_4]_2[PS_4]$), these 12 sites are statistically occupied by 11 Na$^+$ ions, and three vacancies are filled with the $[MS_4]$ (M = Sn, P) tetrahedron with one vacancy left, which is marked by green spheres in Fig. 8b. Moreover, they found that some Na$^+$ occupies the vacancy and considered the position playing a key role for activating the ion migration process.

5.3 Chemical and electrochemical stability

5.3.1 Chemical stability. One of the key issues that limits the applications of chalcogenide-based SEs is their sensitivity to moisture. They are easily hydrolyzed to release H_2S gas since S is a soft Lewis base. The "theory of hard and soft acids and bases" suggests that "hard acids prefer to bind hard bases and soft acids prefer to bind soft bases". Therefore, S forms more stable complexes with soft Lewis acids such as As, Sn, and Sb. However P-based samples prefer to react with oxygen rather than sulfur. Thus most P-based SEs have poor air stability, and the introduction of As, Sn, and Sb into the structure of sulphide electrolytes can improve air stability.[106] Taking Na_3SbS_4 as an example, the air-stability test was performed under an ambient atmosphere for 48 h (humidity 70%). Raman and XRD results (Fig. 8c and d) reveal that Na_3SbS_4 absorbs moisture into sodium thioantimonate hydrate after air-exposure and restoration to the original crystal structure after reheating. Therefore, Na_3SbS_4 is chemically stable in an ambient environment.[56]
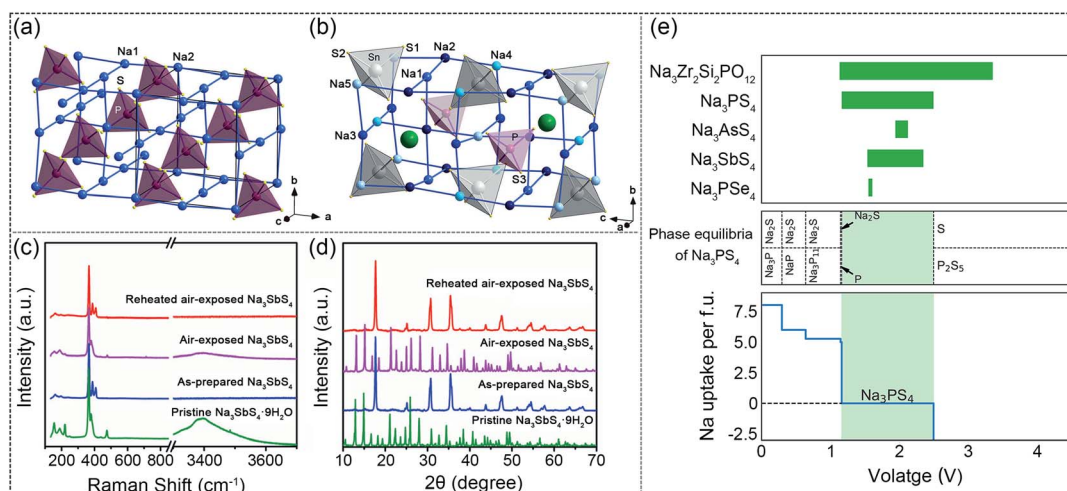

Fig. 8 (a) Na–Na interatomic contacts in the crystal structure of Na_3PS_4; $[PS_4]^{3-}$ tetrahedra and Na$^+$ ions are drawn in dark purple and blue, respectively. (b) Na–Na interatomic contacts in the crystal structure of $Na_{11}Sn_2PS_{12}$. Large green spheres mark unoccupied vacancies in the NbO-type structure formed by the Na$^+$ cations.[65] Reproduced with permission from ref. 65. Copyright (2018), Wiley. Structural evaluations of Na_3SbS_4 before and after air exposure: (c) Raman spectra and (d) XRD patterns of pristine $Na_3SbS_4·9H_2O$, as-synthesized Na_3SbS_4, air-exposed Na_3SbS_4 (48 h), and reheated air-exposed Na_3SbS_4 samples (150 °C for 1 h under vacuum).[56] Reproduced with permission from ref. 56. Copyright (2016), Wiley. (e) Electrochemical stability of the studied solid-state sodium electrolytes (top). Predicted phase equilibria over different voltage (μ_{Na}) ranges for one example solid electrolyte, Na_3PS_4 (middle). The Na uptake per formula unit of Na_3PS_4 vs. voltage (bottom).[105] Reproduced with permission from ref. 105. Copyright (2017), American Chemical Society.

This journal is © The Royal Society of Chemistry 2021

J. Mater. Chem. A, 2021, **9**, 5134–5148 | **5143**

Similar conclusions have also been obtained for other SEs such as, $Na_{4-x}Sn_{1-x}Sb_xS_4$, $Na_{2.88}Sb_{0.88}W_{0.12}S_4$, and $Na_3P_{0.62}As_{0.38}S_4$.[60,62,66]

5.3.2 Electrochemical stability. The electrochemical window of the solid electrolyte is one of the important properties for its application in all-solid-state batteries. Although for most of the chalcogenide-based SEs, the electrochemical window can reach up to 5 V when the CV test is carried out using metallic sodium as the counter electrode and an inert electrode (Pt/Au/In) as the blocking electrode.[51,56,84,97] However, theoretical calculation and battery performance results indicate that the real electrochemical windows of chalcogenide-based SEs are usually overrated, and are relatively narrow especially compared to those of oxide-based solid electrolytes.[105,107,108] Fig. 8e shows the electrochemical windows of some typical chalcogenide-based ISSEs predicted by theoretical simulations.[105] The voltage windows for Na_3PnCh_4 (Pn = P, As, Sb, Ch = S, Se) are between 1 and 2.5 V vs. Na^+/Na. The voltage windows of chalcogenide-based ISSEs are much narrower than those of oxide-based electrolytes. According to the simulated results, Na_3PS_4 decomposes to Na_2S and other Na–P compounds below 1.55 V and is oxidized to form S and P_2S_7 above 2.25 V.[107,109] As for $Na_{11}Sn_2PS_{12}$, the electrochemical decomposition reaction occurs above the voltage of 1.16–1.92 V. The reduction products of Na_2S, Na_3P and $Na_{15}Sn_4$ gradients form when the voltage is below 1.16 V, and the oxidation products, SnS_2, P_2S_7, and S form when the voltage exceeds 1.92 V.[108] Since the CV test is performed with no potential differences in the cell, there is a potential difference in the full solid-state batteries under working conditions. Han et al. proposed a novel experimental method to reflect the electrochemical window by taking inorganic lithium solid electrolytes (ILSEs) of $Li_{10}GeP_2S_{12}$ and Li_7-$La_3Zr_2O_{12}$ as examples.[110] A new kind of test model, a Li/electrolyte/electrolyte-carbon cell, was fabricated to replace the typical Li/electrolyte/inert metal cell. It provides a new method to assess the electrochemical window of ISSEs. In addition,

recent work on sulphide-based ILSEs claimed that metal stability and kinetic stability induced by mechanical constriction may be associated with the difference of voltage windows obtained from the experimental and the simulation results. Similar influence may also exist in sulphide-based ISSEs.[111]

In spite of the alleged narrower electrochemical window, there are still some ASSSBs with decent performance using the reported chalcogenide-based ISSEs.[91,112–116] That is because when in contact with the anode, if the SEs are thermodynamically stable against the anode, a stable interface will form. If the SEs are thermodynamically unstable with the anode, chemical reactions occur between them; the resulting interfacial stability is largely related to the nature of the decomposition products. An electronically insulating but ion conducting interface can help to achieve good electrochemical performance. In contrast, the formation of a mixed-conducting interphase will deteriorate the electrode/electrolyte interface, consume the SEs, increase the interface resistance and cause the growth of dendrites.[109,117] Therein, decomposition products such as Na_2S is a known electronic insulator that is beneficial to ion percolation[73,109] while the other decomposition products, such as $Na_{15}Sn_4$, Na_3P and other electronically conducting substances may conduct both ions and electrons, which is to the disadvantage of interfacial stability.[109] Thus reasonable material design for generating a stable interphase and interfacial engineering could ameliorate electrochemical stability. For traditional battery research, halides are effective constituents to improve the stability of the solid electrolyte interphase (SEI).[118,119] Recently, the experimental results also showed that the electrochemical stability of chalcogenide-based solid electrolytes could be improved by halogen doping.[73,74,120] Introduction of Cl in Na_3PS_4 improves the cyclability of Na_3PS_4-based solid-state sodium batteries due to the fact that Cl-doping can passivate or stabilize the electrode–electrolyte interface.[73] Some research also shows that the electrochemical window can be regulated by microstructural design. To design a core–shell structure Li–Si–P–S
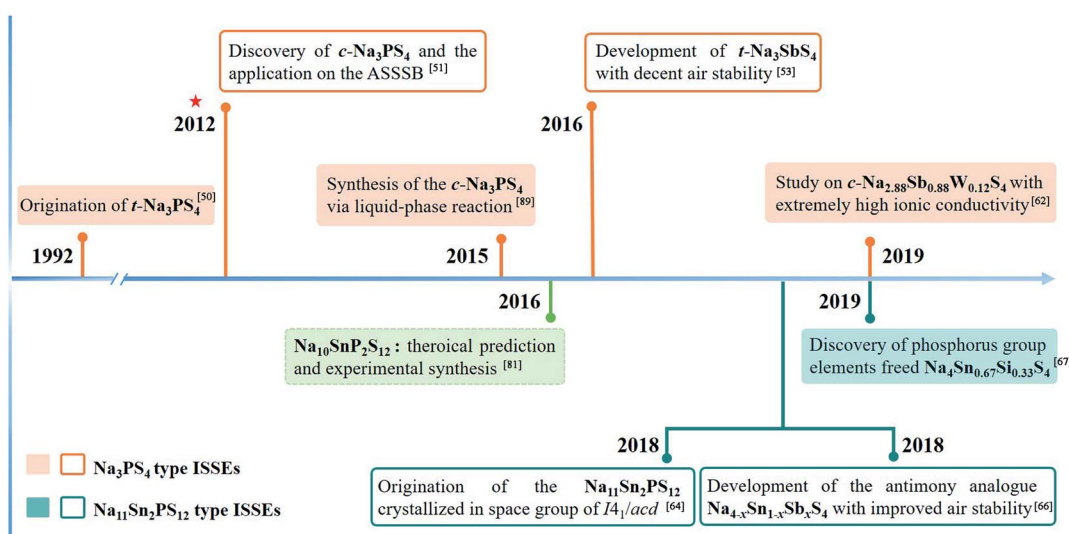

Fig. 9 The timeline figure of several important events in the development of chalcogenide-based ISSEs.

5144 | J. Mater. Chem. A, 2021, **9**, 5134–5148

This journal is © The Royal Society of Chemistry 2021

sulphide electrolyte with a distinct Si composition in the shell, Wu et al. improved the electrochemical stability in the Li–Si–P–S SEs system.[111] The typical method used for interface modification is to construct a protecting layer. Hu et al. demonstrated a cellulose–poly(ethylene oxide) interlayer between Na_3SbS_4 SEs and Na metal to improve the interfacial stability due to the fact that the electron pathway was shut off.[121] On account of the relatively better electrochemical stability of Na_3PS_4 among chalcogenide-based ISSEs, Na_3PS_4 is also used as a modified interface to promote stability between the negative electrode and other solid electrolytes in ASSSBs.[53,66,69]

6.   Summary and outlook

Several important events in the development of chalcogenide-based ISSEs are illustrated in Fig. 9. And combined with the above discussion, chalcogenide-based ISSEs show significant potential for applications in room temperature ASSSBs, though they are a relatively young field in contrast with the traditional oxide-based ISSE system.

More recently, W doped Na_3SbS_4 has been reported to deliver excellent ionic conductivity, even higher than that of current liquid organic electrolytes used for sodium batteries, showing great potential to be used as a solid electrolyte for next-generation solid-state sodium batteries.[62,63] Based on an overview of the reported studies, it was observed that the ionic conductivities of SEs are closely related to the synthesis and testing process, and the recent study in view of their synthesis–property relationship may provide us with more essential understanding of this phenomenon.[95] Nevertheless, many problems still need to be addressed for further exploration of chalcogenide-based ISSEs. For example, (1) the influence of W doping on the electrochemical stability and its application in all-solid-state Na batteries are unclear. (2) The intrinsic mechanism of the improved structure tolerance after the introduction of Si in Na_4SnS_4 needs to be revealed. (3) Halogen doping is considered as an effective strategy to improve the intrinsic electrochemical stability of ISSEs, but few studies using this strategy to improve the electrochemical stability of ISSEs have been reported. What's more, the structure system of chalcogenide-based ISSEs is rarely explored. There are still some potential structures worth exploring. For instance, $Na_7P_3X_{11}$ (X = O, S, Se) was predicted with high room temperature ionic conductivity by first-principles calculations but not explored in experiment until now.[122] Argyrodite-type lithium-based SEs are widely studied, while no sodium analogues are synthesized or predicted. Hence the basic understanding of structural evolution is essential.

The present review summarizes research on chalcogenide-based ISSEs mainly based on the crystal structure. Not only the synthetic routes to obtain chalcogenide-based ISSEs are systematically summarized, but also the structural characteristics, factors that affect the Na^+ diffusion process, chemical/electrochemical stability, and structure–activity relationships of $Na_{3-y-z}P_{1-x}Pn_xW_yCh_{4-z}X_z$ (Pn = Sb, As; Ch = S, Se; X = Cl), $Na_{11}Sn_2PnCh_{12}$ and $Na_{12-x-y}[Sn_2Si]_{1-x}Pn_xS_{12-y}X_y$ (Pn = P, Sb; X = Cl, Br, I) systems are discussed based on current theoretical

calculations and experimental research results. Last but not least, structural correlations are emphasized in this review to unravel the fundamental mechanism of ISSEs and guide the targeted design of high-performance ISSEs.

Conflicts of interest

There are no conflicts to declare.

Acknowledgements

References

1 M. D. Slater, D. Kim, E. Lee and C. S. Johnson, *Adv. Funct. Mater.*, 2013, **23**, 947–958.

2 D. Kundu, E. Talaie, V. Duffort and L. F. Nazar, *Angew. Chem., Int. Ed.*, 2015, **54**, 3431–3448.

3 B. L. Ellis and L. F. Nazar, *Curr. Opin. Solid State Mater. Sci.*, 2012, **16**, 168–177.

4 V. Palomares, P. Serras, I. Villaluenga, K. B. Hueso, J. Carretero-González and T. Rojo, *Energy Environ. Sci.*, 2012, **5**, 5884.

5 C. Delmas, *Adv. Energy Mater.*, 2018, **8**, 1703137.

6 C.-H. Dustmann, *J. Power Sources*, 2004, **127**, 85–92.

7 R. J. Bones, D. A. Teagle, S. D. Brooker and F. L. Cullen, *J. Electrochem. Soc.*, 1989, **136**, 1274–1277.

8 Y.-F. Y. Yao and J. T. Kummer, *J. Inorg. Nucl. Chem.*, 1967, **29**, 2453–2475.

9 Y. Wang, D. Zhou, V. Palomares, D. Shanmukaraj, B. Sun, X. Tang, C. Wang, M. Armand, T. Rojo and G. Wang, *Energy Environ. Sci.*, 2020, **13**, 3848.

10 K. B. Hueso, M. Armand and T. Rojo, *Energy Environ. Sci.*, 2013, **6**, 734–749.

11 Z. Man, P. Li, D. Zhou, Y. Wang, X. Liang, R. Zang, P. Li, Y. Zuo, Y. M. Lam and G. Wang, *Nano Lett.*, 2020, **20**, 3769–3777.

12 C. Zhao, L. Liu, X. Qi, Y. Lu, F. Wu, J. Zhao, Y. Yu, Y.-S. Hu and L. Chen, *Adv. Energy Mater.*, 2018, **8**, 1703012.

13 J. Motavalli, *Nature*, 2015, **526**, s96–s97.

14 Y.-S. Hu, *Nat. Energy*, 2016, **1**, 16042–16043.

15 K. B. Hueso, V. Palomares, M. Armand and T. Rojo, *Nano Res.*, 2017, **10**, 4082–4114.

16 X. Xu, K. Lin, D. Zhou, Q. Liu, X. Qin, S. Wang, S. He, F. Kang, B. Li and G. Wang, *Chem*, 2020, **6**, 902–918.

17 Q. Zhao, S. Stalin, C.-Z. Zhao and L. A. Archer, *Nat. Rev. Mater.*, 2020, **5**, 229–252.

18 Z. Zhang, Y. Shao, B. Lotsch, Y.-S. Hu, H. Li, J. Janek, L. F. Nazar, C.-W. Nan, J. Maier, M. Armand and L. Chen, *Energy Environ. Sci.*, 2018, **11**, 1945–1976.

19 C. Zhou, S. Bag and V. Thangadurai, *ACS Energy Lett.*, 2018, **3**, 2181–2198.

20 L. Peng, H. Jia, Q. Ding, Y. Zhao, J. Xie and S. Cheng, *Energy Storage Sci. Technol.*, 2020, **9**, 1370–1382.

This journal is © The Royal Society of Chemistry 2021

J. Mater. Chem. A, 2021, **9**, 5134–5148 | **5145**

21 J. B. Goodenough, H. Y.-P. Hong and J. A. Kafalas, *Mater. Res. Bull.*, 1976, **11**, 203–220.

22 H. Y.-P. Hong, *Mater. Res. Bull.*, 1976, **11**, 173–182.

23 T. Takahashi and K. Kuwabara, *J. Appl. Electrochem.*, 1980, **10**, 291–297.

24 Y. I. L. Viswanathan and A. V. Virkar, *J. Mater. Sci.*, 1983, **18**, 109–113.

25 S. N. Heavens, *J. Mater. Sci.*, 1988, **23**, 3515–3518.

26 S.-T. Lee, D.-H. Lee, S.-M. Lee, S.-S. Han, S.-H. Lee and S.-K. Lim, *Bull. Mater. Sci.*, 2016, **39**, 729–735.

27 Y. Wang, S. Song, C. Xu, N. Hu, J. Molenda and L. Lu, *Nano Mater. Sci.*, 2019, **1**, 91–100.

28 N. S. Bell, C. Edney, J. S. Wheeler, D. Ingersoll, E. D. Spoerke and P. Gouma, *J. Am. Ceram. Soc.*, 2014, **97**, 3744–3748.

29 J. F. Ihlefeld, E. Gurniak, B. H. Jones, D. R. Wheeler, M. A. Rodriguez, A. H. McDaniel and B. Dunn, *J. Am. Ceram. Soc.*, 2016, **99**, 2729–2736.

30 H. Park, K. Jung, M. Nezafati, C.-S. Kim and B. Kang, *ACS Appl. Mater. Interfaces*, 2016, **8**, 27814–27824.

31 S. Song, H. M. Duong, A. M. Korsunsky, N. Hu and L. Lu, *Sci. Rep.*, 2016, **6**, 32330.

32 M. Guin, S. Indris, M. Kaus, H. Ehrenberg, F. Tietz and O. Guillon, *Solid State Ionics*, 2017, **302**, 102–106.

33 Y. Ruan, S. Song, J. Liu, P. Liu, B. Cheng, X. Song and V. Battaglia, *Ceram. Int.*, 2017, **43**, 7810–7815.

34 S. Wang, H. Xu, W. Li, A. Dolocan and A. Manthiram, *J. Am. Chem. Soc.*, 2017, **140**, 250–257.

35 M. Matsuo, S. Kuromoto, T. Sato, H. Oguchi, H. Takamura and S.-i. Orimo, *Appl. Phys. Lett.*, 2012, **100**, 203904–203907.

36 Y. Wang, Q. Wang, Z. Liu, Z. Zhou, S. Li, J. Zhu, R. Zou, Y. Wang, J. Lin and Y. Zhao, *J. Power Sources*, 2015, **293**, 735–740.

37 J. Zhu, Y. Wang, S. Li, J. W. Howard, J. Neuefeind, Y. Ren, H. Wang, C. Liang, W. Yang, R. Zou, C. Jin and Y. Zhao, *Inorg. Chem.*, 2016, **55**, 5993–5998.

38 Z.-L. Lv, H.-L. Cui, H. Wang, X.-H. Li and G.-F. Ji, *Phys. Status Solidi B*, 2017, **254**, 1700089.

39 T. H. Wan, Z. Lu and F. Ciucci, *J. Power Sources*, 2018, **390**, 61–70.

40 Y. Sun, Y. Wang, X. Liang, Y. Xia, L. Peng, H. Jia, H. Li, L. Bai, J. Feng, H. Jiang and J. Xie, *J. Am. Chem. Soc.*, 2019, **141**, 5640–5644.

41 H. Oguchi, M. Matsuo, S. Kuromoto, H. Kuwano and S. Orimo, *J. Appl. Phys.*, 2012, **111**, 036102–036104.

42 T. J. Udovic, M. Matsuo, W. S. Tang, H. Wu, V. Stavila, A. V. Soloninin, R. V. Skoryunov, O. A. Babanova, A. V. Skripov, J. J. Rush, A. Unemoto, H. Takamura and S.-i. Orimo, *Adv. Mater.*, 2014, **26**, 7622–7626.

43 W. S. Tang, M. Matsuo, H. Wu, V. Stavila, A. Unemoto, S.-i. Orimo and T. J. Udovic, *Energy Storage Mater.*, 2016, **4**, 79–83.

44 W. S. Tang, K. Yoshida, A. V. Soloninin, R. V. Skoryunov, O. A. Babanova, A. V. Skripov, M. Dimitrievska, V. Stavila, S.-i. Orimo and T. J. Udovic, *ACS Energy Lett.*, 2016, **1**, 659–664.

45 L. Duchêne, R. S. Kühnel, E. Stilp, E. Cuervo Reyes, A. Remhof, H. Hagemann and C. Battaglia, *Energy Environ. Sci.*, 2017, **10**, 2609–2615.

46 B. R. S. Hansen, M. Paskevicius, M. Jørgensen and T. R. Jensen, *Chem. Mater.*, 2017, **29**, 3423–3430.

47 Y. Sadikin, P. Schouwink, M. Brighi, Z. Łodziana and R. Černý, *Inorg. Chem.*, 2017, **56**, 5006–5016.

48 J. A. Dawson, P. Canepa, M. J. Clarke, T. Famprikis, D. Ghosh and M. S. Islam, *Chem. Mater.*, 2019, **31**, 5296–5304.

49 S. Ohno, A. Banik, G. F. Dewald, M. A. Kraft, T. Krauskopf, N. Minafra, P. Till, M. Weiss and W. G. Zeier, *Prog. Energy*, 2020, **2**, 022001.

50 M. Jansen and U. Henseler, *J. Solid State Chem.*, 1992, **99**, 110–119.

51 A. Hayashi, K. Noi, A. Sakuda and M. Tatsumisago, *Nat. Commun.*, 2012, **3**, 856.

52 A. Hayashi, K. Noi, N. Tanibata, M. Nagao and M. Tatsumisago, *J. Power Sources*, 2014, **258**, 420–423.

53 A. Banerjee, K. H. Park, J. W. Heo, Y. J. Nam, C. K. Moon, S. M. Oh, S.-T. Hong and Y. S. Jung, *Angew. Chem., Int. Ed.*, 2016, **55**, 9634–9638.

54 L. Zhang, D. Zhang, K. Yang, X. Yan, L. Wang, J. Mi, B. Xu and Y. Li, *Adv. Sci.*, 2016, **3**, 1600089.

55 D. Zhang, X. Cao, D. Xu, N. Wang, C. Yu, W. Hu, X. Yan, J. Mi, B. Wen, L. Wang and L. Zhang, *Electrochim. Acta*, 2018, **259**, 100–109.

56 H. Wang, Y. Chen, Z. D. Hood, G. Sahu, A. S. Pandian, J. K. Keum, K. An and C. Liang, *Angew. Chem., Int. Ed.*, 2016, **55**, 8551–8555.

57 L. Zhang, K. Yang, J. Mi, L. Lu, L. Zhao, L. Wang, Y. Li and H. Zeng, *Adv. Energy Mater.*, 2015, **5**, 1501294–1501298.

58 S.-H. Bo, Y. Wang and G. Ceder, *J. Mater. Chem. A*, 2016, **4**, 9044–9053.

59 N. Wang, K. Yang, L. Zhang, X. Yan, L. Wang and B. Xu, *J. Mater. Sci.*, 2017, **53**, 1987–1994.

60 Z. Yu, S.-L. Shang, J.-H. Seo, D. Wang, X. Luo, Q. Huang, S. Chen, J. Lu, X. Li, Z.-K. Liu and D. Wang, *Adv. Mater.*, 2017, **29**, 1605561–1605567.

61 S.-L. Shang, Z. Yu, Y. Wang, D. Wang and Z.-K. Liu, *ACS Appl. Mater. Interfaces*, 2017, **9**, 16261–16269.

62 A. Hayashi, N. Masuzawa, S. Yubuchi, F. Tsuji, C. Hotehama, A. Sakuda and M. Tatsumisago, *Nat. Commun.*, 2019, **10**, 5266–5271.

63 T. Fuchs, S. P. Culver, P. Till and W. G. Zeier, *ACS Energy Lett.*, 2019, **5**, 146–151.

64 Z. Zhang, E. Ramos, F. Lalère, A. Assoud, K. Kaup, P. Hartman and L. F. Nazar, *Energy Environ. Sci.*, 2018, **11**, 87–93.

65 M. Duchardt, U. Ruschewitz, S. Adams, S. Dehnen and B. Roling, *Angew. Chem., Int. Ed.*, 2018, **57**, 1351–1355.

66 J. W. Heo, A. Banerjee, K. H. Park, Y. S. Jung and S.-T. Hong, *Adv. Energy Mater.*, 2018, **8**, 1702716.

67 H. Jia, Y. Sun, Z. Zhang, L. Peng, T. An and J. Xie, *Energy Storage Mater.*, 2019, **23**, 508–513.

68 H. Jia, X. Liang, T. An, L. Peng, J. Feng and J. Xie, *Chem. Mater.*, 2020, **32**, 4065–4071.

5146 | *J. Mater. Chem. A*, 2021, **9**, 5134–5148

This journal is © The Royal Society of Chemistry 2021

69 H. Jia, L. Peng, Z. Zhang, T. An and J. Xie, *J. Energy Chem.*, 2020, **48**, 102–106.

70 T. Famprikis, P. Canepa, J. A. Dawson, M. S. Islam and C. Masquelier, *Nat. Mater.*, 2019, **18**, 1278–1291.

71 M. Jansen, *Angew. Chem., Int. Ed.*, 1991, **30**, 1547–1558.

72 R. C. Agrawal and R. K. Gupta, *J. Mater. Sci.*, 1999, **34**, 1131–1162.

73 I.-H. Chu, C. S. Kompella, H. Nguyen, Z. Zhu, S. Hy, Z. Deng, Y. S. Meng and S. P. Ong, *Sci. Rep.*, 2016, **6**, 33733.

74 E. A. Wu, C. S. Kompella, Z. Zhu, J. Z. Lee, S. C. Lee, I.-H. Chu, H. Nguyen, S. P. Ong, A. Banerjee and Y. S. Meng, *ACS Appl. Mater. Interfaces*, 2018, **10**, 10076–10086.

75 N. Tanibata, K. Noi, A. Hayashi, N. Kitamura, Y. Idemoto and M. Tatsumisago, *ChemElectroChem*, 2014, **1**, 1130–1132.

76 S. Takeuchi, K. Suzuki, M. Hirayama and R. Kanno, *J. Solid State Chem.*, 2018, **265**, 353–358.

77 R. P. Rao, H. Chen, L. L. Wong and S. Adams, *J. Mater. Chem. A*, 2017, **5**, 3377–3388.

78 C. K. Moon, H.-J. Lee, K. H. Park, H. Kwak, J. W. Heo, K. Choi, H. Yang, M.-S. Kim, S.-T. Hong, J. H. Lee and Y. S. Jung, *ACS Energy Lett.*, 2018, **3**, 2504–2512.

79 X. Feng, P.-H. Chien, Z. Zhu, I.-H. Chu, P. Wang, M. Immediato-Scuotto, H. Arabzadeh, S. P. Ong and Y.-Y. Hu, *Adv. Funct. Mater.*, 2019, **29**, 1807951–1807959.

80 F. Tsuji, S. Yubuchi, A. Sakuda, M. Tatsumisago and A. Hayashi, *J. Ceram. Soc. Jpn.*, 2020, **128**, 641–647.

81 W. D. Richards, T. Tsujimura, L. J. Miara, Y. Wang, J. C. Kim, S. P. Ong, I. Uechi, N. Suzuki and G. Ceder, *Nat. Commun.*, 2016, **7**, 11009.

82 F. Tsuji, N. Tanibata, A. Sakuda, A. Hayashi and M. Tatsumisago, *Chem. Lett.*, 2018, **47**, 13–15.

83 M. Duchardt, S. Neuberger, U. Ruschewitz, T. Krauskopf, W. G. Zeier, J. Schmedt auf der Günne, S. Adams, B. Roling and S. Dehnen, *Chem. Mater.*, 2018, **30**, 4134–4139.

84 Z. Yu, S.-L. Shang, Y. Gao, D. Wang, X. Li, Z.-K. Liu and D. Wang, *Nano Energy*, 2018, **47**, 325–330.

85 N. Tanibata, K. Noi, A. Hayashi and M. Tatsumisago, *RSC Adv.*, 2014, **4**, 17120–17123.

86 S. Yubuchi, A. Ito, N. Masuzawa, A. Sakuda, A. Hayashi and M. Tatsumisago, *J. Mater. Chem. A*, 2020, **8**, 1947–1954.

87 T. W. Kim, K. H. Park, Y. E. Choi, J. Y. Lee and Y. S. Jung, *J. Mater. Chem. A*, 2018, **6**, 840–844.

88 M. Uematsu, S. Yubuchi, F. Tsuji, A. Sakuda, A. Hayashi and M. Tatsumisago, *J. Power Sources*, 2019, **428**, 131–135.

89 S. Yubuchi, A. Hayashi and M. Tatsumisago, *Chem. Lett.*, 2015, **44**, 884–886.

90 M. Ghidiu, J. Ruhl, S. P. Culver and W. G. Zeier, *J. Mater. Chem. A*, 2019, **7**, 17735–17753.

91 H. Wan, J. P. Mwizerwa, X. Qi, X. Liu, X. Xu, H. Li, Y.-S. Hu and X. Yao, *ACS Nano*, 2018, **12**, 2809–2817.

92 N. J. J. de Klerk and M. Wagemaker, *Chem. Mater.*, 2016, **28**, 3122–3130.

93 T. Krauskopf, S. P. Culver and W. G. Zeier, *Inorg. Chem.*, 2018, **57**, 4739–4744.

94 Z. Zhu, I.-H. Chu, Z. Deng and S. P. Ong, *Chem. Mater.*, 2015, **27**, 8318–8325.

95 T. Famprikis, Ö. U. Kudu, J. A. Dawson, P. Canepa, F. Fauth, E. Suard, M. Zbiri, D. Dambournet, O. J. Borkiewicz, H. Bouyanfif, S. P. Emge, S. Cretu, J.-N. Chotard, C. P. Grey, W. G. Zeier, M. S. Islam and C. Masquelier, *J. Am. Chem. Soc.*, 2020, **142**, 18422–18436.

96 S.-H. Bo, Y. Wang, J. C. Kim, W. D. Richards and G. Ceder, *Chem. Mater.*, 2015, **28**, 252–258.

97 N. Kamaya, K. Homma, Y. Yamakawa, M. Hirayama, R. Kanno, M. Yonemura, T. Kamiyama, Y. Kato, S. Hama, K. Kawamoto and A. Mitsui, *Nat. Mater.*, 2011, **10**, 682–686.

98 V. S. Kandagal, M. D. Bharadwaj and U. V. Waghmare, *J. Mater. Chem. A*, 2015, **3**, 12992–12999.

99 E. P. Ramos, Z. Zhang, A. Assoud, K. Kaup, F. Lalère and L. F. Nazar, *Chem. Mater.*, 2018, **30**, 7413–7417.

100 Z. Zhang, P.-N. Roy, H. Li, M. Avdeev and L. F. Nazar, *J. Am. Chem. Soc.*, 2019, **141**, 19360–19372.

101 A. Sorkin and S. Adams, *Mater. Adv.*, 2020, **1**, 184–196.

102 M. A. Kraft, L. M. Gronych, T. Famprikis, S. Ohno and W. G. Zeier, *Chem. Mater.*, 2020, **32**, 6566–6576.

103 T. Krauskopf, S. Muy, S. P. Culver, S. Ohno, O. Delaire, Y. Shao-Horn and W. G. Zeier, *J. Am. Chem. Soc.*, 2018, **140**, 14464–14473.

104 T. Krauskopf, C. Pompe, M. A. Kraft and W. G. Zeier, *Chem. Mater.*, 2017, **29**, 8859–8869.

105 H. Tang, Z. Deng, Z. Lin, Z. Wang, I.-H. Chu, C. Chen, Z. Zhu, C. Zheng and S. P. Ong, *Chem. Mater.*, 2017, **30**, 163–173.

106 G. Sahu, Z. Lin, J. Li, Z. Liu, N. Dudney and C. Liang, *Energy Environ. Sci.*, 2014, **7**, 1053–1058.

107 Y. Tian, T. Shi, W. D. Richards, J. Li, J. C. Kim, S.-H. Bo and G. Ceder, *Energy Environ. Sci.*, 2017, **10**, 1150–1166.

108 K. Oh, D. Chang, I. Park, K. Yoon and K. Kang, *Chem. Mater.*, 2019, **31**, 6066–6075.

109 S. Wenzel, T. Leichtweiss, D. A. Weber, J. Sann, W. G. Zeier and J. Janek, *ACS Appl. Mater. Interfaces*, 2016, **8**, 28216–28224.

110 F. Han, Y. Zhu, X. He, Y. Mo and C. Wang, *Adv. Energy Mater.*, 2016, **6**, 1501590–1501598.

111 F. Wu, W. Fitzhugh, L. Ye, J. Ning and X. Li, *Nat. Commun.*, 2018, **9**, 4037.

112 J. Yue, X. Zhu, F. Han, X. Fan, L. Wang, J. Yang and C. Wang, *ACS Appl. Mater. Interfaces*, 2018, **10**, 39645–39650.

113 X. Fan, J. Yue, F. Han, J. Chen, T. Deng, X. Zhou, S. Hou and C. Wang, *ACS Nano*, 2018, **12**, 3360–3368.

114 X. Chi, Y. Liang, F. Hao, Y. Zhang, J. Whiteley, H. Dong, P. Hu, S. Lee and Y. Yao, *Angew. Chem., Int. Ed.*, 2018, **57**, 2630–2634.

115 N. Tanibata, M. Deguchi, A. Hayashi and M. Tatsumisago, *Chem. Mater.*, 2017, **29**, 5232–5238.

116 F. Hao, X. Chi, Y. Liang, Y. Zhang, R. Xu, H. Guo, T. Terlier, H. Dong, K. Zhao, J. Lou and Y. Yao, *Joule*, 2019, **3**, 1349–1359.

This journal is © The Royal Society of Chemistry 2021

J. Mater. Chem. A, 2021, **9**, 5134–5148 | **5147**

117 G. G. Eshetu, G. A. Elia, M. Armand, M. Forsyth, S. Komaba, T. Rojo and S. Passerini, *Adv. Energy Mater.*, 2020, **10**, 2000093.

118 X. Ji, S. Hou, P. Wang, X. He, N. Piao, J. Chen, X. Fan and C. Wang, *Adv. Mater.*, 2020, **32**, 2002741.

119 X. Zhao, Z. Zhao-Karger, M. Fichtner and X. Shen, *Angew. Chem., Int. Ed.*, 2020, **59**, 5902–5949.

120 F. Han, J. Yue, X. Zhu and C. Wang, *Adv. Energy Mater.*, 2018, **8**, 1703644–1703649.

121 P. Hu, Y. Zhang, X. Chi, K. Kumar Rao, F. Hao, H. Dong, F. Guo, Y. Ren, L. C. Grabow and Y. Yao, *ACS Appl. Mater. Interfaces*, 2019, **11**, 9672–9678.

122 Y. Wang, W. D. Richards, S.-H. Bo, L. J. Miara and G. Ceder, *Chem. Mater.*, 2017, **29**, 7475–7482.